JOURNAL OF GEOPHYSICAL RESEARCH, VOL. ???, XXXX, DOI:10.1029/,

Tandem afterslip on connected fault planes following the 2008 Nima-Gaize (Tibet) earthquake

I. Ryder

Department of Earth and Ocean Sciences, University of Liverpool, 4

Brownlow St, Liverpool, UK, L69 3GP

R. Bürgmann

Berkeley Seismological Laboratory, McCone Hall, UC Berkeley, CA 94704

J. Sun

State Key Laboratory of Earthquake Dynamics, Institute of Geology, China

Earthquake Administration

I. Ryder, Department of Earth and Ocean Sciences, University of Liverpool, 4 Brownlow St, Liverpool, UK, L69 3GP (i.ryder@liv.ac.uk)

Abstract.

On 9 January 2008 a M 6.4 normal-faulting earthquake occurred in central Tibet, near the border of Nima and Gaize counties and just north of the Bangong-Nujiang suture zone. A week later, a M 5.9 aftershock occurred a few kilometers to the northwest of the mainshock. Here we consider InSAR data from the Japanese ALOS and European Envisat satellites, covering both the coseismic phase and 9 months of postseismic deformation. The coseismic interferograms clearly show surface deformation resulting from both mainshock and aftershock ruptures, and data inversions using elastic dislocation models suggest that two northwest-dipping faults form a synthetic system, with the more steeply-dipping aftershock plane meeting the mainshock plane at depth. Postseismic interferograms show first order similarities with their coseismic counterparts, indicating that afterslip occurred on both mainshock and aftershock rupture surfaces during the months following the earthquakes. The afterslip occurred at comparable depths to the coseismic slip, but the amount of slip was about an order of magnitude smaller. A slip template method is used to obtain moment release estimates at different postseismic time intervals, and hence document the time dependence of the postseismic transient. The exponential decay time of the afterslip is 34 days, and the moment release due to the afterslip was about 10 % of the coseismic moment. Models of viscoelastic stress relaxation in a Maxwell half space place a strong lower bound on mid to lower crustal viscosity of 3×10^{17} Pa s. Postseismic data covering a longer time span have the potential to improve this constraint.

1. Introduction

The counties of Nima and Gaize are situated in central Tibet, just north of the Bangong suture zone. Tectonically, this is an area characterized by EW-trending thrust faults and folds related to the late Jurassic-early Cretaceous collision of the Lhasa and Qiangtang terranes, and subsequent shortening during mid-Cretaceous and mid-Tertiary times [*DeCelles et al.*, 2007]. The initial collision involved southward emplacement of the Qiangtang terrane over the Lhasa terrane, the sediments of the intervening ocean basin forming the Bangong suture zone [*Kapp et al.*, 2005]. Thrust faults within the suture zone were reactivated during continued north-south convergence, and the south-dipping Gaize-Siling Co backthrust, which marks the southern boundary of the suture zone, formed during the Tertiary. Active north-south shortening and east-west extension in southern and central Tibet are accommodated by NS-trending normal faults and conjugate strike-slip faults [e.g. *Armijo et al.*, 1989; *Taylor et al.*, 2003].

The 9 January 2008 earthquake occurred near the western end of the ENE-WSW-trending left-lateral Riganpei Co fault (Figure 1), which is the northern branch of one of these conjugate strike-slip systems. The event ruptured a zone of Jurassic flysch/limestone deposits and volcanics [*Kapp et al.*, 2005] on the northern side of the Riganpei Co fault. *Taylor and Peltzer* [2006] used InSAR to estimate a slip rate of 6 ± 2 mm/yr on this fault, and a present day east-west rate of extension for this region of 13 mm/yr. *Sun et al.* [2008] presented coseismic Envisat data for the Nima-Gaize event, and inferred that two separate northwest-dipping normal faults ruptured. They identified these faults with the

mainshock and largest aftershock, which occurred one week later and approximately 7 km to the northwest of the mainshock.

In this paper we present InSAR data which document both coseismic and postseismic deformation associated with the Nima-Gaize earthquake. In addition to the Envisat coseismic data considered in *Sun et al.* [2008], we use new Envisat and ALOS data which document coseismic rupture followed by postseismic deformation for several months following the initial seismic events. We perform inversions for coseismic distributed slip using four coseismic interferograms, all of which have excellent coherence. In addition, a single early postseismic interferogram is inverted for distributed afterslip. To estimate the time dependence of deformation over the postseismic observation interval so far, a slip template method is employed, in which the slip distribution obtained in the coseismic inversion is used as a template for postseismic slip during different time intervals. To place constraints on the viscosity of the mid to lower crust, we compute first order models of viscoelastic stress relaxation and compare with InSAR observations.

2. Mainshock and aftershocks

The M 6.4 normal-faulting mainshock occurred on 9 January 2008. The scalar moment according to the Global Centroid Moment Tensor (CMT) catalog was 5.02×10^{18} N m. During the rest of January, 44 aftershocks with M>3.2 occurred, and subsequently there were no seismic events above magnitude 3 until mid-April. The largest (M 5.9) aftershock occurred on 16 January at 11:54 GMT. The exact timing of this aftershock is important, because one of the SAR scenes used in this study was taken about five hours later on the same day. The aftershock's scalar moment was estimated to be 8.66×10^{17} N m, which

gives a total combined moment for both events of 5.88×10^{18} N m. The locations of the mainshock and largest aftershock according to both the National Earthquake Information Center (NEIC) and the CMT catalogs are offset from the location of the surface ruptures inferred from the InSAR data. In Figure 2, the CMT and NEIC catalog locations are shifted in the (east, north) directions by (0.002°, 0.139°) and (0.113°, 0.174°), respectively, so that the mainshock of each set overlies the center of the InSAR-derived fault trace at 6 km depth (corresponding to the centroid of the CMT case) or 12 km depth (NEIC case). After this translation, the largest aftershock in both datasets lies at the northern end of the secondary fault trace as inferred from the InSAR data. The smaller aftershocks show significant positional discrepancy between the two datasets, but the shifted CMT aftershocks are significantly less scattered than the NEIC events. In the following analysis and throughout this paper, we prinicipally use source parameters from the Global CMT catalog. Aside from the largest aftershock, the only other CMT event with M>5 during the first month was a M 5.5 event on 22 January, with a moment release of 1.90×10^{17} N m. It should be noted that besides two M 4.9 aftershocks on the 14 and 17 January recorded in the CMT catalog, the NEIC recorded two additional sizeable aftershocks, a M 5.0 on the day of the mainshock and a M 4.9 on 11 January.

3. InSAR data

In this study we use synthetic aperture radar (SAR) data from both the Japanese Advanced Land Observing Satellite (ALOS) and European Envisat satellite. The incidence angle of the ALOS SAR acquisitions was 38° and that of the Envisat images was 23° (beam mode 2, otherwise called IS2) or 41° (beam mode 6, or IS6). Scene coverage for each satellite is shown on the location map of Figure 1. The data are processed using

the open source ROIPAC software developed at Caltech/JPL [*Rosen et al.*, 2004]. Topographic fringes in the phase component are removed using the 90 m Shuttle Radar Topography Mission (SRTM) digital elevation model (DEM) [*Farr et al.*, 2007]. The time chart in Figure 3 shows the temporal coverage of the coseismic and postseismic differential interferograms, along with their perpendicular baselines. Also marked are the times of seismic events with M≥4.9, for reference.

3.1. Coseismic inteferograms

We use the descending and ascending Envisat interferograms presented in the coseismic study of *Sun et al.* [2008], and an alternative Envisat ascending interferogram from Track 427 with more comprehensive coverage of the deformed area than that from Track 341 used in the previous study. All three interferograms cover through the start of February 2008, with second acquisition dates within six days of each other. In addition, we use an ascending ALOS coseismic interferogram constructed from a pair of SAR scenes acquired three months apart on 16 October 2007 and 16 January 2008. This image covers both the mainshock and primary aftershock, but unlike the two Envisat images does not cover the following two to three postseismic weeks. The four interferograms are shown in Figure 4a–d. The excellent coherence and generally low atmospheric noise level in the interferograms allow a clear view of the surface deformation field associated with the earthquakes. Also marked in Figure 4 are the locations of two northwest-dipping fault surface traces constrained by the deformation patterns in the InSAR data (see Section 4 for discussion of fault geometry). The large bullseye pattern of positive range change seen in all four interferograms represents motion away from the satellite in the hanging wall (western side) of the mainshock, a significant component of which is subsidence across the

normal fault. On the footwall (eastern) side, a change in sign of line-of-sight deformation is seen in the descending interferogram, but not in the ascending images. This is a result of the different viewing geometries, and the way the horizontal and vertical components of displacement project into the line-of-sight between the satellite and the ground. The smaller bullseye embedded within the larger fringe pattern represents motion in the hangingwall of the largest aftershock. As discussed in Section 4, slip on the mainshock alone is not sufficient to reproduce the nested bullseye pattern, but slip on both the mainshock and aftershock together can reproduce the observed deformation [*Sun et al.*, 2008].

A fifth interferogram is shown in Figure 4e. This ALOS ascending image covers the mainshock and aftershock, and also six months of postseismic deformation. The overall pattern of range change is the same as that in the other ascending images, but the magnitude of the range change is almost 10 % greater than in the purely coseismic ALOS interferogram (number 3). This increase is consistent with the patterns of surface deformation in the postseismic interferograms discussed next.

3.2. Postseismic interferograms

From nine months of Envisat and ALOS SAR data, we were able to construct six postseismic interferograms, both ascending and descending (Figure 5). ALOS interferograms numbers 7 and 10 (see timeline in Figure 3) required a post-processing correction to remove long wavelength phase banding across the images, described in the Supplementary Material. Interferogram 6, produced from an ascending ALOS pair, shows marked similarity to the coseismic ALOS interferogram, as illustrated by the wrapped image in the top right panel of Figure 5. Again there is a nested bullseye, and a far-field deformation

lobe in the hanging wall beyond the bullseye. This similarity of coseismic and postseismic interferograms suggests that a similar subsurface process occurred during both phases; specifically, it suggests that the dominant postseismic process over the observation period is afterslip on the two faults that ruptured initially. Other postseismic processes such as poroelastic rebound and viscoelastic relaxation would be expected to give rather different spatial patterns of surface deformation (see Section 5 and Section 7). Number 9 is an ascending interferogram produced from Envisat IS2 scenes with a different look angle (23°), so the spatial pattern is different in detail from the ALOS images, but the first order pattern is consistent, i.e. a region of positive range change to the northwest of the mainshock rupture. The two independent descending Envisat interferograms (nos. 8 and 11) also share common features, in particular a lobe of negative range change to the east of the mainshock surface trace and a zone of positive range between the two surfaces traces. The spatial pattern of the descending interferograms is different from the ascending ones, due to the different satellite-ground geometry. In this case, a change in sign of the line-of-sight displacements is seen across each fault structure (see Figure 5c). This sign change is observed in both coseismic and postseismic images, which again supports the scenario that the postseismic deformation is due to afterslip. A qualitative idea of the time dependence of the postseismic transient can be gained from examination of the six interferograms, particularly those with the same satellite viewing geometry. Comparison of the ALOS ascending images (numbers 6 and 10), for example, indicates that the positive range change lobe attributed to afterslip has several times greater magnitude during the first 1.5 months compared to the three subsequent months.

Despite an order of magnitude difference in range change, a striking first order similarity exists between the shapes of the coseismic and postseismic line-of-sight displacement profiles taken perpendicular to the fault traces (Figure 6). The location of the fault traces (gray lines) can be readily identified from dips and discontinuities in the profiles. Also evident is the footwall sign contrast between descending and ascending profiles. Since the amplitude of postseismic deformation is over an order of magnitude smaller than the coseismic deformation, the postseismic images have a much lower signal-to-noise ratio, and so the postseismic profiles are not as smooth. However, the coseismic and postseismic profiles have approximately the same overall shape and wavelength as the coseismic equivalent, implying that afterslip occurred on the same two fault planes as the coseismic slip and extended about as deep as the initial slip.

4. Inversions for distributed slip

In this section we perform inversions for distributed slip on a pair of fault planes corresponding to the rupture surfaces of the mainshock and primary aftershock. First we jointly invert the first four coseismic interferograms (Figure 4a–d), noting that the three Envisat images include three to four weeks of postseismic deformation. We then invert the earliest postseismic ALOS interferogram, whose start date is a few hours after the largest aftershock, and whose total temporal coverage is 1.5 months. Despite the noise level in the interferogram being of comparable magnitude to the tectonic signal, performing this single early postseismic inversion gives a first order insight into the distribution of afterslip.

4.1. Coseismic inversions

We aim to determine the optimal geometry and distribution of slip on the two fault planes that ruptured in the mainshock and largest aftershock. Prior to the coseismic inversion, downsampling of the unwrapped coseismic interferograms is carried out using the quadtree decomposition method [*Jónsson et al.*, 2002]. This is an adaptive approach that averages pixel values over larger areas where the image gradient is low, and smaller areas where the image gradient is high. Since the deformation gradients in this case are up to an order of magnitude greater than gradients of noise in the interferogram, a quadtree threshold can be chosen easily such the deforming area is densely sampled and non-deforming areas are sparsely sampled. Following resampling of the interferograms, Green's functions are computed, which relate unit slip on individual fault patches to surface displacements at individual observation points [*Okada*, 1985]. For the Green's function calculations, the value of both Lamé elastic parameters is 33 GPa and Poisson's ratio is 0.25. The faults are discretized into patches which are 2 km in both along-strike and down-dip directions. We vary fault strike and dip in different inversions, but in any one solution, strike and dip are held fixed. We solve for rake and slip magnitude on each patch. Green's functions are computed for two different rakes, $-45°$ and $-135°$, and model parameters are estimated by non-negative least squares optimization in Matlab, such that the slip vectors fall within $\pm 45°$ of pure normal. Each interferogram is weighted using covariance matrices derived from the autocorrelation function of non-deforming regions. Laplacian smoothing is applied to avoid large, unphysical variations in slip values between adjacent patches. The optimal smoothing parameter is estimated by plotting root mean square (rms) misfit against solution roughness and selecting the smoothing value

corresponding to the large change in gradient at the elbow, i.e. the value beneath which roughness increases significantly and beyond which the rms misfit rises steeply (Figure 7).

We take as a starting point the fault geometry determined by *Sun et al.* [2008] from analysis of a different set of coseismic Envisat InSAR data. Whereas they determined their fault geometry using uniform slip inversions, and then proceeded to run distributed slip inversions with fixed fault geometry, we prefer to explore fault geometry using distributed slip inversions. We explore different possible dip and strike angles, varying the angles independently at 2° intervals between 30° and 60° (dip) and 190° and 230° (strike). We also adjust the location of the center of the surface fault traces to try and minimize near-field residuals. For each combination of trial parameters, Green's functions are computed as described above. The results of the coseismic inversion are shown in Figure 9. The observed unwrapped interferograms are displayed in the left-hand panels, the optimal model displacements projected into the appropriate line-of-sight are displayed in the middle column, and the residuals are shown in the right-hand panels. The optimal model successfully reproduces the essential features of the coseismic deformation field. However, near-field residuals are obtained for all four interferograms. Their magnitude is small (note the different color scale used for the residuals relative to the original data and models), but their consistency across the four interferograms suggests a systematic shortcoming of the model geometry. One possibility is the constant length of the modeled fault plane at different depths. Experimentation with changing the along-strike length of the fault planes suggests that some of the near-field residual (Figure 9) is a result of slip midway along the fault plane being smeared out along-strike in the top few kilometers. Alternatively, it is possible that the faults are actually curved, as suggested by the shape

of the discontinuities in range change in three of the postseismic interferograms (numbers 8, 9 and 11).

Our optimal fault parameters are listed in Table 1. In summary, this geometry consists of two faults which converge at depth and have slightly oblique strike directions (see Figure 8). The mainshock plane extends from the surface down to a depth of 16 km, while the aftershock plane extends from the surface down to 10 km depth. The rms misfit for this combination of source parameters is 2.9 cm. Maximum slip of 1.10 m occurs at 6–8 km depth for the mainshock and up to 0.61 m of slip is found at 2–4 km depth for the aftershock. The moment release on the mainshock and aftershock planes combined is 5.90×10^{18} Pa s, close to the CMT combined scalar moment of 5.88×10^{18} Pa s. Errors in the slip distribution are estimated by generating 100 sets of realistic noise from the autocorrelation functions of the non-deforming regions of each interferogram, and adding this noise to the corresponding interferogram. The inversion is then re-run for each perturbed dataset, and the errors shown in Figure 8 are the standard deviations of the slip values for each patch obtained in the 100 inversions.

We tested whether or not two faults are required to explain the observations, by performing an inversion using only the mainshock plane of the optimal two-fault model, and adjusting fault geometry parameters according to the same grid-based scheme as previously described for the two-fault model. The synthetic interferograms from the best-fit single fault solutions cannot reproduce the nested bullseye pattern, and give large residuals in the area of the primary aftershock fault trace. We are confident, then, that the coseismic interferograms record offset across both mainshock and primary aftershock faults. We also explored a listric fault geometry using a three fault configuration, with two shallow

steeply-dipping faults connecting with a shallow-dipping third fault at depth. However, the lowest misfit to the data with this configuration was slightly higher than that using our optimal two fault scenario, so we can say that the data do not require a listric geometry, though they also do not rule one out. The best solution may be given by "spoon-shaped" faults, which as well as having listric character could reduce the near-field residuals seen in Figure 9.

4.2. Postseismic inversion

The postseismic interferograms record surface deformation whose amplitude is an order of magnitude smaller than that in the coseismic interferograms. Collectively, the postseismic images show that the amplitude of the tectonic signal decreases rapidly during the first few postseismic months. Here we invert the earliest postseismic interferogram (no. 6) for afterslip on the mainshock and aftershock fault planes. Since the magnitude of the postseismic tectonic signal is of the same order as the estimated noise in the interferogram (standard deviation 0.49 cm), quadtree decomposition is not appropriate, since it would potentially sample some areas of noise as densely as areas of signal. Instead, downsampling on a regular grid is implemented, using bicubic sampling to preserve the smoothness of the original signal. This yields 1756 points, with a pixel spacing of $\sim$1.4 km. To allow for the possibility of both shallow and deep afterslip, the fault geometry is modified slightly from the coseismic inversions, in that the mainshock plane is extended down to a depth of 20 km, and the aftershock plane is extended to 11 km depth - any deeper would cause it to intersect with the mainshock plane.

The results of the postseismic inversion are shown in Figure 10. The slip distribution has a zone of shallow (< 10 km) normal slip on each fault plane, similar to the coseismic distribution. Most of the slip occurs on the aftershock plane, which reflects the larger line-of-sight displacement west of the aftershock trace relative to the eastern side. This may be a result of noise in the interferogram overprinting the tectonic signal, since later postseismic interferograms (numbers 8 and 9) suggest that an equal or greater amount of slip occurred on the mainshock plane relative to the aftershock plane. The deep slip with oblique rake on the mainshock plane may be apparent slip, representing another process other than afterslip occurring at depth such as viscoelastic stress relaxation, or it may be an artifact caused by noise in the interferogram. For example, the lobe of negative range change at the southern end of the mainshock fault is likely localized phase difference due to tropospheric water vapor present on one or both of the satellite acquisition dates. In summary, the postseismic inversion results support the inference of afterslip, and indicate that its amplitude is about an order of magnitude smaller than that of the coseismic slip. The moment release of the afterslip distribution is 1.17×10^{18} N m. However, we note that the signal in the interferogram is about the same order of magnitude as the noise. We include the inversion results here to demonstrate the potential challenges of using postseismic data directly when the signal-to-noise ratio is rather low, and to better justify our use of the slip template method for analysing postseismic time dependence (Section 6).

5. Poroelastic modeling

In this section we investigate whether any features of the postseismic interferograms or the residuals obtained in the coseismic/postseismic inversions can be explained by

poroelastic rebound during the early postseismic period. A poroelastic mechanism has been proposed to explain, for example, postseismic motion following the 1992 Landers earthquake [*Peltzer et al.*, 1998] and a pair of earthquakes in the south Iceland seismic zone [*Jónsson et al.*, 2003]. According to this mechanism, surface ground motion is caused by the flow of fluid driven by earthquake-induced pore pressure gradients. The initial undrained and final drained conditions of the rock can be modeled by higher and lower values of Poisson's ratio respectively [*Rice and Cleary*, 1976]. Surface displacements are computed using coseismic dislocation models with both values of Poisson's ratio, and the difference between the displacement fields represents the poroelastic rebound. The difference in undrained and drained values in postseismic studies is typically about 0.04 [*Peltzer et al.*, 1998].

Performing this calculation using the slip distribution obtained in the coseismic inversion, an undrained Poisson's ratio of 0.29, and a drained ratio of 0.25, gives the results shown in Figure 11. In this figure, the components of motion are projected into Envisat/ALOS ascending and descending satellite geometries, for ease of comparison with the interferograms in Figure 4 and Figure 5, and the residual fields in Figure 9. The similarity between descending and ascending models indicates that vertical motion is the dominant component of displacement. The pattern of positive range change residual in the mainshock footwall in the ascending images is comparable to the poroelastic model, but the magnitude of the model displacement is about five times smaller than in the residual field. The modeled descending displacements bear very little resemblance to the corresponding residual field, nor to the postseismic residual. Furthermore, the pattern of surface displacement in the poroelastic model predictions is not evident in any of the

postseismic interferograms. We conclude that poroelastic rebound alone is not sufficient to explain the interferometric observations or the inversion residuals, though there may be some small poroelastic contribution to postseismic deformation during the first few weeks.

6. Time dependence of postseismic deformation

Although there are too few interferograms to allow construction of a full pixel-by-pixel displacement time series, we investigate the overall time evolution of moment release due to afterslip during the postseismic observation period. The coseismic slip distribution obtained in Section 4.1 is used to generate a template surface displacement field, and a scaling factor is sought for each separate time interval which best matches the predicted displacement field to the observed field during that period. This approach makes the assumption that the slip distribution is spatially unvarying between coseismic and postseismic phases. The similarity in overall shape and wavelength of the coseismic and postseismic surface displacement patterns (Figure 6) argues for a similar depth of slip in both coseismic and afterslip phases. We choose not to use the postseismic inversion result as a template because tropospheric water vapor likely has a significant signature in the postseismic InSAR data (see discussion in Section 4.2). In choosing to use the coseismic slip model, we do not assert that the distribution of slip is necessarily identical for coseismic and postseismic phases. Since detailed differences in the actual slip patterns are unresolvable with the current dataset, the coseismic model represents an approximation to the true afterslip distribution, which nonetheless explains the key features of the observed displacement field.

The scaling factors which best match the observed displacements to the coseismic template (Figure 12) are converted to differential moment release during the various time intervals, using the coseismic moment release for calibration. The moment release values at the start and end of each interval are plotted against their respective time spans, using the redundancy of dates in the dataset to yield a time series (Figure 13). The best-fit exponential curve through these points has a decay time of 34 days, i.e. much of the afterslip occurs during the first month following the inital seismic rupture, and the afterslip is essentially complete by the end of the first year. The total postseismic moment release due to afterslip is about 10 % of the seismic moment. We note that the total moment contributed by all aftershocks smaller than the M 5.9 event is only a few per cent of the aseismic moment release inferred geodetically, and so these smaller shocks cannot account for the observed postseismic surface displacements. Interferograms 8 through 11 have start dates from February 2008 onwards, i.e. after the majority of aftershocks occurred, and yet a tectonic signal is still observed in these images.

7. Viscoelastic modeling

The viscosity of the lower crust beneath the central Tibetan plateau is not well-established, and geodetic observations of postseismic motion offer an opportunity to probe the viscosity structure beneath the elastic upper crust. For earthquakes where the spatial pattern of postseismic deformation is consistent with viscoelastic relaxation, models can be used to estimate an optimal viscosity from the data [e.g. *Nishimura and Thatcher*, 2003; *Ryder et al.* , 2007]. In the present case, the postseismic interferograms do not show a clear viscoelastic relaxation signal. For an upper crustal normal fault which ruptures to the surface, modeling of stress-driven postseismic relaxation in a viscoelastic medium be-

neath the seismogenic layer indicates that broadly-distributed uplift is expected over the faulted area during the transient phase [e.g. *Nishimura and Thatcher*, 2003]. This uplift occurs as material flows in towards the faulted area in response to the shear stress changes and overlying redistribution of upper crustal material during the earthquake. The uplift would be seen in the interferograms as an approximately circular zone of negative range change over the faults (Figure 14). In the absence of such a signal, we estimate a lower bound on mid-crustal viscosity by running simple models of viscoelastic relaxation, with an elastic upper crust and a Maxwell half space beneath. Values of elastic lid thickness used are 14 km and 20 km; the former is chosen to be a little deeper than the hypocentral depth of the CMT solution (13.3 km). The viscosity of the Maxwell half space is varied between 10^{16} and 10^{19} Pa s. Using the slip distribution on both faults obtained in the coseismic inversion (Figure 8) as input to the model, the line-of-sight displacement field at the surface is computed for the time intervals of five of the postseismic interferograms (numbers 6, 8, 9, 10 and 11). Number 7 is not used since it is effectively a sum of numbers 6 and 10. For each viscosity, the root mean square (rms) difference between the residuals obtained in the scaling exercise described above (Section 6) and modeled viscoelastic displacements is computed. The viscosity beneath which the rms misfit value starts to rise steeply represents a lower bound on Maxwell viscosity. Errors in the rms misfit values are estimated by adding realistic noise to the residuals using the method described in Section 4.1 for the coseismic interferograms, and running the best-fit calculation 100 times. The errors plotted in Figure 14 are the standard deviations of the rms misfit distributions.

The images in Figure 14 show modeled displacements for each of the five time interferogram time intervals, projected into the appropriate line-of-sight for that interferogram.

For these model calculations, a viscosity of 3×10^{17} Pa s was used. Of the residuals in Figure 12, that of interferogram number 9 (080216-080426) shows the greatest similarity with the viscoelastic model prediction, but at this point in the observational history the data are lacking clear, unambiguous evidence for viscoelastic relaxation. The bottom right panel in Figure 14 displays the misfit between residuals and model outputs as a function of viscosity, for the two values of elastic lid thickness. The lower bound obtained is 3×10^{17} Pa s, which is independent of lid thickness. Since the misfit falls rapidly at lower viscosities, and the estimated errors in the rms values are small, this lower bound is a robust constraint on the mid to lower crustal viscosity for this part of Tibet.

8. Discussion

This paper adds to the small number of studies investigating postseismic surface deformation following normal faulting earthquakes. Such studies have great potential for determining the mechanism of postseismic stress relaxation, since for dip-slip events, the surface displacement field due to localized afterslip and distributed viscous flow at depth are spatially very different. *Nishimura and Thatcher* [2003] modeled leveling data covering almost three decades after the 1959 M_w 7.3 Hebgen Lake, Montana normal faulting event, using both afterslip and viscoelastic relaxation scenarios. They found that the observed broad pattern of postseismic uplift required viscoelastic relaxation in the upper mantle with a viscosity of 4×10^{18} Pa s, but near-field short wavelength features of the measured displacement field were explained by shallow afterslip in the upper 2 km of the crust. The authors also showed that the data rule out a model of deep afterslip on a down-dip extension of the coseismic faults. Analysis of a four-year GPS postseismic dataset for the 1997 Umbria-Marche, Italy earthquake sequence was carried out by *Riva et al.* [2007].

The optimal model obtained was a combination of afterslip occurring both on a shallow up-dip extension of the two coseismic rupture planes and on a horizontal plane at the base of the seismogenic upper crust, and viscoelastic relaxation in a layer with Maxwell viscosity 10^{18} Pa s. It is of interest that these two case studies, like the present one, involve coseismic slip and associated afterslip on a pair of synthetic normal faults. In the case of Nima-Gaize, however, the afterslip occurred on the fault plane from the surface down to the depth of coseismic slip, rather than being limited to the very shallow upper crust, and substantial slip on a deep downdip extension of the coseismic rupture can be ruled out. Our preliminary examination of postseismic InSAR data for three other normal faulting earthquakes that occurred in Tibet during 2008 (Yutian on 20 March, Zhongba on 25 August and Damxung on 6 October) reveals localized deformation in each case, suggesting that shallow afterslip may be the norm for such events.

The firm lower bound on mid-crustal viscosity obtained in Section 7 is of interest in the context of the large range of viscosity values obtained for the mid to lower crust of Tibet in different analyses. Several modeling studies which aim to rationalize the present-day topography of Tibet argue for a weak mid and/or lower crust beneath the plateau as a whole, with viscosities ranging from 10^{16} to 10^{20} Pa s [e.g. *Clark and Royden*, 2000; *Shen et al.*, 2001; *Clark and Royden*, 2008; *Bendick et al.*, 2008]. A small number of studies have used geodetic data to place quantitative constraints on the viscosity of the mid crust beneath smaller sub-areas of the plateau, acknowledging that the rheological structure may vary laterally. *Copley and McKenzie* [2007], for instance, use present-day GPS surface velocities to estimate a crustal viscosity of of 10^{20} Pa s for southern Tibet. *Hilley et al.* [2009] considered both the Kunlun and the Altyn Tagh faults in a modeling study of

GPS data from northern Tibet which takes into account time-dependent earthquake cycle effects. They infer viscosities greater than 10^{18} Pa s for the mid to lower crust of this part of Tibet.

Occasional moderate to large earthquakes on the Tibetan plateau present opportunities for investigating rheological structure with much denser spatial and temporal geodetic coverage than the interseismic studies mentioned above. *Ryder et al.* [2007] performed an InSAR study of postseismic deformation following the 1997 M_w 7.6 Manyi earthquake. For a viscoelastic relaxation model, they inferred effective viscosity values of about 3-10×10^{18} Pa s below 15 km depth, noting that the observed postseismic signal can also be explained by a plausible afterslip distribution. Our preliminary analysis of geodetic data following the 2001 M_w 7.9 Kokoxili earthquake on the Kunlun fault suggests that the most appropriate characterization of a viscoelastic lower crust in northeast Tibet is a Burgers rheology, with transient and steady-state viscosities in the range 10^{18}-5×10^{19} Pa s. Such a rheology is also consistent with the Manyi InSAR time series.

For central Tibet, a lack of suitable earthquakes until 2008 means that postseismic motion has until now not been studied geodetically to yield viscosity estimates. The Nima-Gaize earthquake therefore represents a first opportunity to characterize the mid-crustal rheology of central Tibet. The estimated lower bound of 3×10^{17} Pa s is smaller than values obtained in the other geodetic studies mentioned above. This may reflect a true lower viscosity in central Tibet relative to the northern and southern regions, or it may be that this lower bound will be pushed higher with a longer observational period. The other moderate-sized normal-faulting earthquakes which have occurred on the central to

southern Tibetan plateau since the Nima-Gaize event offer a wider-reaching opportunity to learn about the rheological structure of the Tibetan crust.

9. Conclusions

We present new coseismic and postseismic InSAR data for the January 2008 Nima-Gaize earthquake which complement the Envisat coseismic interferograms considered by *Sun et al.* [2008]. The coseismic data clearly indicate surface offset across a pair of synthetic normal faults, which elastic dislocation modeling shows to be linked at depth. Following *Sun et al.* [2008], we identify these ruptures with the M 6.4 mainshock on 9 January and the M 5.9 aftershock on 16 January. Inversion for the coseismic slip distribution yields up to 1.10 m of slip on the mainshock plane and up to 61 cm of slip on the aftershock plane, though it should be noted that a small amount of this is likely early afterslip on the mainshock plane. The six postseismic interferograms show consistently that shear offset continued to occur across both rupture surfaces. The pattern of surface deformation is very similar to that observed in the coseismic interferograms, and indicates that afterslip extended from the surface down to a similar depth to the coseismic rupture, but very deep afterslip on a down-dip extension of the coseismic ruptures is not indicated. We use a slip template method to estimate the moment release during different postseismic time intervals, and construct a time series of postseismic moment release. The exponential decay time for this time series is 34 days, with afterslip being essentially complete by the end of the first year, and releasing about 10 % of the coseismic moment. Modeling of viscoelastic relaxation in a Maxwell half space enables us to place a robust lower bound of 3×10^{17} Pa s on the effective viscosity of the mid to lower crust of central Tibet. Continued monitoring of the postseismic transient should enable us to improve on this constraint.

Acknowledgments.

This work is supported by NSF award EAR 0738298. Envisat data were made available by the European Space Agency (ESA), and ALOS data were obtained from the Japan Aerospace Exploration Agency (JAXA).

References

Armijo, R., P. Tapponnier, and T.-L. Han (1989), Late Cenozoic right-lateral strike-slip faulting in southern Tibet, *J. Geophys. Res.*, **94 (B3)**, 2787–2838.

Bendick, R., D. McKenzie, and J. Etienne (2008), Topography associated with crustal flow in continental collisions, with application to Tibet, *Geophys. J. Int.*, **175(1)**, 375–385.

Clark, M. K., and L. H. Royden (2000), Topographic ooze: Building the eastern margin of Tibet by lower crustal flow, *Geology*, **28(8)**, 703–706.

Cook, K. L., and L. H. Royden (2008), The role of crustal strength variations in shaping orogenic plateaus, with application to Tibet, *J. Geophys. Res.*, **113**, doi:10.1029/2007JB005457.

Copley, A., and D. McKenzie (2007), Models of crustal flow in the India-Asia collision zone, *Geophys. J. Int.*, **169(2)**, 683–698.

DeCelles, P. G., P. Kapp, L. Ding, and G. E. Gehrels (2007), Late Cretaceous to middle Tertiary basin evolution in the central Tibetan Plateau: Changing environments in response to tectonic partitioning, aridification, and regional elevation gain, *GSA Bulletin*, **119**, 654–680.

Farr, T. G. *et al.* (2007), The Shuttle Radar Topography Mission, *Rev. Geophys.*, **45**, doi:10.1029/2005RG000183.

Freed, A. M., and R. Bürgmann (2004), Evidence of power-law flow in the Mojave desert mantle, *Nature*, **430**, 548–551.

Hilley, G., K. M. Johnson, M. Wang, Z.-K. Shen, and R. Bürgmann (2009), Earthquake-cycle deformation and fault slip rates in northern Tibet, *Geology*, **37(1)**, 31–34.

Jónsson, S., H. Zebker, P. Segall, and F. Amelung (2002), Fault slip distribution of the Mw 7.2 Hector mine earthquake estimated from satellite radar and GPS measurements, *Bull. Seismol. Soc. Am.*, **92**, 1377–1389.

Jónsson, S., P. Segall, R. Pedersen, and G. Björnsson (2003), Post-earthquake ground movements correlated to pore-pressure transients, *Nature*, **424**, 179–183.

Kapp, P., A. Yin, T. M. Harrison, and L. Ding (2005), Cretaceous-Tertiary shortening, basin development, and volcanism in central Tibet, *GSA Bulletin*, **117**, 865–878.

Nishimura, T., and W. Thatcher (2003), Rheology of the lithosphere inferred from post-seismic uplift following the 1959 Hebgen Lake earthquake, *J. Geophys. Res.*, **108**, doi:10.1029/2002JB002191.

Okada, Y. (1985), Surface deformation due to shear and tensile faults in a half-space, *Bull. Seismol. Soc. Am.*, **75 (4)**, 1135-1154.

Peltzer, G., P. Rosen, F. Rogez, and K. Hudnut (1998), Poroelastic rebound along the Landers 1992 earthquake surface rupture, *J. Geophys. Res.*, **103, B12**, 30131–30145.

Rice, J. R., and M. P. Cleary (1976), Some basic stress diffusion solutions for fluid-saturated elastic porous media with compressible constituents, *Rev. Geophysics and Space Phy.*, **14**, 227–241.

Riva, R. E. M., A. Borghi, A. Aoudia, R. Barzarghi, R. Sabadini, and G. F. Panza (2007), Viscoelastic relaxation and long-lasting after-slip following the 1997 Umbria-Marche

(Central Italy) earthquakes, *Geophys. J. Int.*, **169**, 534–546.

Rosen, P. A., S. Hensley, and G. Peltzer (2004), Updated Repeat Orbit Interferometry Package Released, *Eos Trans. AGU*, **85**, 35.

Ryder, I., B. E. Parsons, T. Wright, and G. Funning (2007), Postseismic motion following the 1997 Manyi (Tibet) earthquake: InSAR observations and modeling, *Geophys. J. Int.*, **169**, 1009–1027.

Shen, F., L. H. Royden, and B. C. Burchfiel (2001), Large-scale crustal deformation of the Tibetan Plateau,*J. Geophys. Res.*, 106, 6793–6816.

Sun, J., Z. Shen, X. Xu, and R. Bürgmann (2008), Synthetic Normal faulting of the January 9, 2008 Nima (Tibet) Earthquake from Conventional and Along-track SAR Interferometry, *Geophys. Res. Lett.*, **35** L22308.

Taylor, M., S. Yin, F. J. Ryerson, P. Kapp, and L. Ding (2003), Conjugate strike-slip faulting along the Bangong-Nujiang suture zone accommodates coeval east-west extension and north-south shortening in the interior of the Tibetan Plateau, *Tectonics*, **22**, doi:10.1029/2002TC001361.

Taylor, M., and G. Peltzer (2006), Current slip rates on conjugate strike-slip faults in central Tibet using synthetic aperture radar, *J. Geophys. Res.*, **111**, doi:10.1029/2005JB004014.

Fault	Latitude (degrees)	Longitude (degrees)	Strike (degrees)	Dip (degrees)	Length (km)	Top (km)	Bottom (km)
(InSAR) this study							
Mainshock	32.411	85.356	214	38	24	0	16
Aftershock	32.440	85.290	204	50	22	0	10
NEIC							
Mainshock	32.288	85.166	204	43	-	-	-
Aftershock	32.331	85.158	220	50	-	-	-
CMT							
Mainshock	32.300	85.320	206	46	-	-	-
Aftershock	32.350	85.290	198	46	-	-	-

Table 1. Optimal fault parameters used in the coseismic distributed slip inversion (top), along with source parameters from the NEIC and CMT earthquake catalogs. For the InSAR case, latitude and longitude are the coordinates of the center of each surface fault trace.

Figure 1. Topographic map of the Nima-Gaize region in central Tibet, with location shown in inset. Shaded relief topography is the SRTM DEM at 90 m resolution. Yellow lines show faults mapped by *Kapp et al.* [2005], and thin black lines (highlighted by thick arrow in center of image) mark mainshock and aftershock fault traces determined from InSAR. Gray boxes mark locations of the ALOS and Envisat SAR tracks used in this study. All Envisat tracks are IS2 except Track 427, which is IS6 and therefore has a smaller swath width. The white dashed box delineates area of surface deformation shown in Figure 4.

Figure 2. Relative aftershock locations from the CMT (red) and NEIC (blue) catalogs. Black lines are surface fault traces inferred from the InSAR data. Each set of event locations is shifted relative to the catalog so that the M 6.4 mainshock (triangles with crosses) is coincident with the InSAR-derived fault center (CMT case) or middle of the lower edge (NEIC case). Smaller crosses within circles denote the largest aftershock. Dates of seismic events are given next to each symbol in mmdd format, and the number beneath the date is the moment magnitude.

Figure 3. Timeline of coseismic and postseismic interferograms used in the present study. Each bar represents a single interferogram, and start and end dates are given above each bar in the format yymmdd. B is perpendicular orbit baseline. The T numbers before each bar are the track numbers; A = ascending, D = descending; star denotes Envisat IS6, otherwise Envisat interferograms are IS2. The mainshock (red bar) and aftershocks with M$\geq$4.9 (blue bars) are marked above the time axis, and reproduced further up the diagram for clarity.

Figure 4. Coseismic interferograms covering both the mainshock on 9 January 2008 and the largest aftershock a week later on 16 January 2008. Interferograms in a to d also cover 3–4 weeks of postseismic deformation; image e covers an additional 6 months of postseismic deformation. Start and end dates are given above each image using the format yymmdd. Phase is re-wrapped such that each fringe represents 10 cm motion in the line of sight between satellite and ground. Black lines are fault traces of model dislocations at the surface. A and A' mark ends of a fault-perpendicular profile along which line-of-sight displacements are displayed in Figure 6.

Figure 5. Postseismic ALOS and Envisat interferograms, collectively covering nine months from immediately after the largest aftershock. Black lines show fault traces. Top right is a wrapped version of the boxed area (white outline) in top left image. Interferogram numbers refer to the numbering scheme in Figure 3. No. 9 is displayed in the Supplementary Material. Dates are given in yymmdd format, and track numbers are also given in each title. A = ascending, D = descending.

Figure 6. Line-of-sight displacement profiles taken through coseismic (top) and postseismic (bottom) interferograms along the line A-A' in Figure 4. Left: ALOS ascending (incidence angle 38°); center: Envisat descending (incidence angle 23°); right: Envisat ascending (incidence angle 41° for Track 427 and 23° for Track 69). Gray lines mark locations of mainshock and aftershock fault planes.

Figure 7. Determination of smoothing factor for the coseismic inversion. The smoothing factor is the value (1800) which corresponds to the elbow of each rms-roughness curve, as explained in the main text.

Figure 8. Results of inversion of all four coseismic interferograms shown in Figure 4. Top panel shows slip magnitudes on the 3-D two fault geometry. Beneath this are flat representations of each fault plane, with slip vectors plotted in addition to the slip magnitude shown in color. Lower panels show slip errors estimated by perturbing the interferogram multiple times with realistic correlated noise, as explained in the main text.

Figure 9. Comparison of coseismic InSAR data with forward models generated using the inverted slip distribution shown in Figure 8. The interferograms are shown left and the model predictions shown in the center column. Note that the residuals (right) are shown with a different color scale.

Figure 10. Results of postseismic inversion (080116-080302). Top panel shows slip magnitudes, and beneath this are flat representations of each fault plane, with slip vectors plotted in addition to the slip magnitude. Third row shows estimated slip errors. Lower panel shows interferogram, forward model and residual.

Figure 11. Results of poroelastic modeling. The slip distribution from the coseismic inversion is used as input to the elastic dislocation models run with different values of Poisson's ratio (0.29 and 0.25 for undrained and drained cases respectively), and the resulting components of surface motion are projected into the Envisat descending (top) and ascending (bottom) line of sight. Black lines mark fault traces.

Figure 12. Comparison of original postseismic interferograms (left) and scaled synthetic interferograms (center), along with the associated residuals (right). The scaled synthetics are generated using the slip model from the coseimic inversion (see Section 4.1), and finding the scaling factor that gives the best fit between data and synthetic. Numbers on the model predictions are the scaling values obtained. Dates for each time interval are given in yymmdd format.

Figure 13. Time series obtained using the template method described in the main text. The moment values for different time intervals are denoted by pairs of different-colored symbols. The grey curve is the best-fitting exponential through the points, with a decay time of 34 days.

Figure 14. Results of viscoelastic model calculations. First five panels in color show modeled surface displacements for the time intervals of interferograms 5, 7, 8, 9 and 10, using a lower crustal viscosity of 3×10^{17} Pa s. The modeled x, y and z components of displacement are projected into the line-of-sight appropriate to the corresponding interferogram. Bottom right panel shows misfit between residuals from the scaling procedure in Section 6 and model displacements, as a function of viscosity. A lower bound of $3{\times}10^{17}$ Pa s can be placed on the viscosity of the mid to lower crust beneath the central Tibetan plateau.

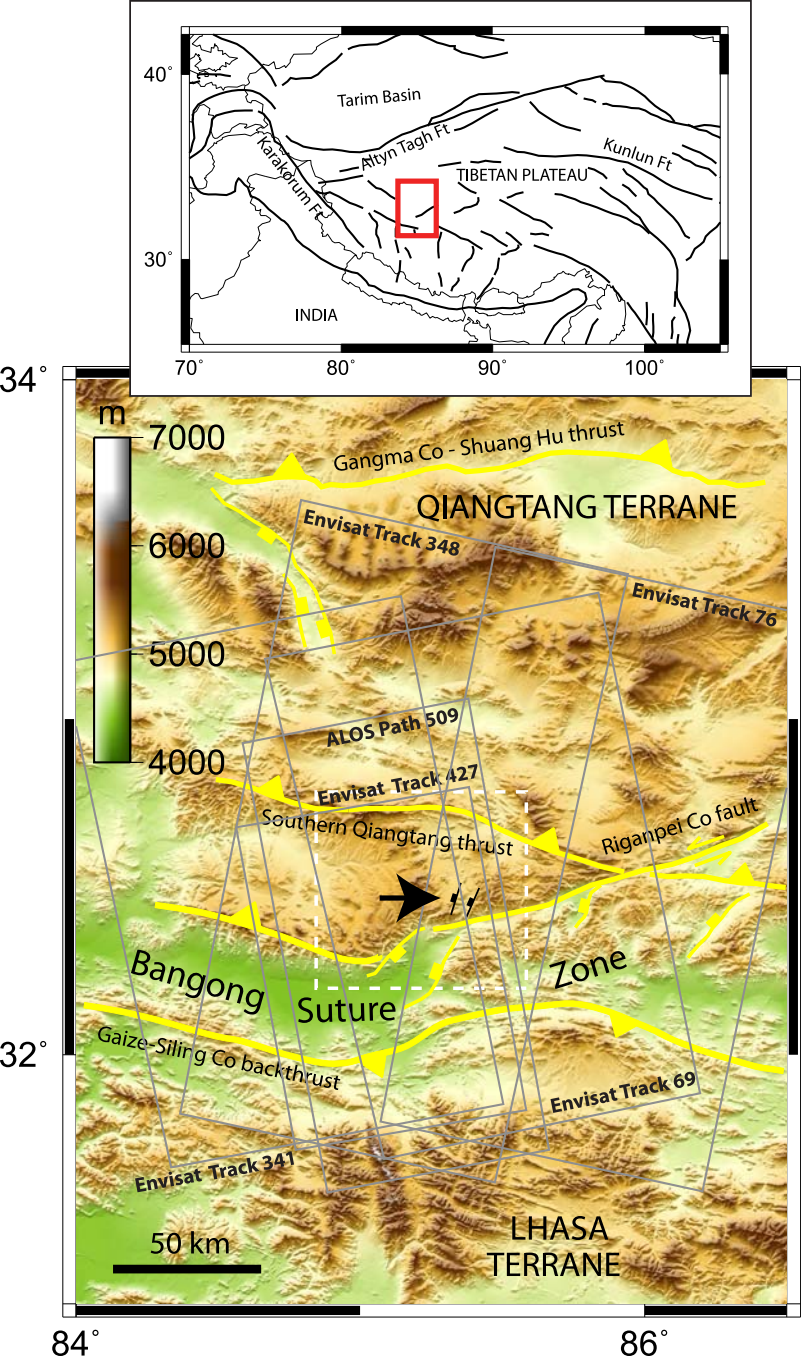
40°
30°
Tarim Basin
Altyn Tagh Ft
Karakorum Ft
TIBETAN PLATEAU
Kunlun Ft
INDIA
70°
80°
90°
100°
34°
m
7000
6000
5000
4000
Gangma Co - Shuang Hu thrust
QIANGTANG TERRANE
Envisat Track 348
Envisat Track 76
ALOS Path 509
Envisat Track 427
Southern Qiangtang thrust
Riganpei Co fault
Bangong
Suture
Zone
32°
Gaize-Siling Co backthrust
Envisat Track 69
Envisat Track 341
50 km
LHASA
TERRANE
84°
86°

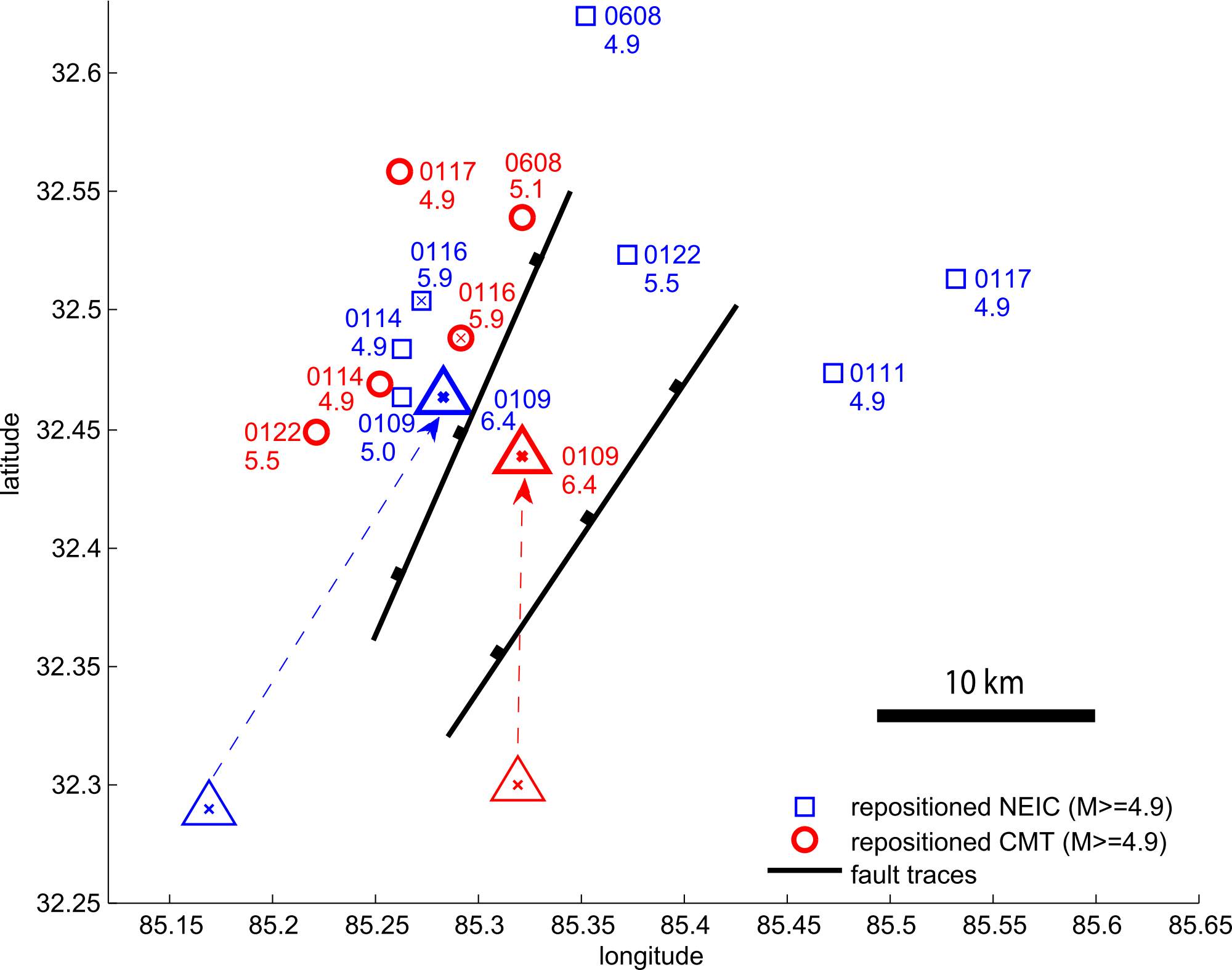
0608
4.9
0117
4.9
0608
5.1
0116
5.9
0122
5.5
0117
4.9
0116
5.9
0114
4.9
0111
4.9
0114
4.9
0109
6.4
0122
5.5
0109
5.0
0109
6.4
10 km
repositioned NEIC (M>=4.9)
repositioned CMT (M>=4.9)
fault traces
latitude
longitude
32.6
32.55
32.5
32.45
32.4
32.35
32.3
32.25
85.15
85.2
85.25
85.3
85.35
85.4
85.45
85.5
85.55
85.6
85.65

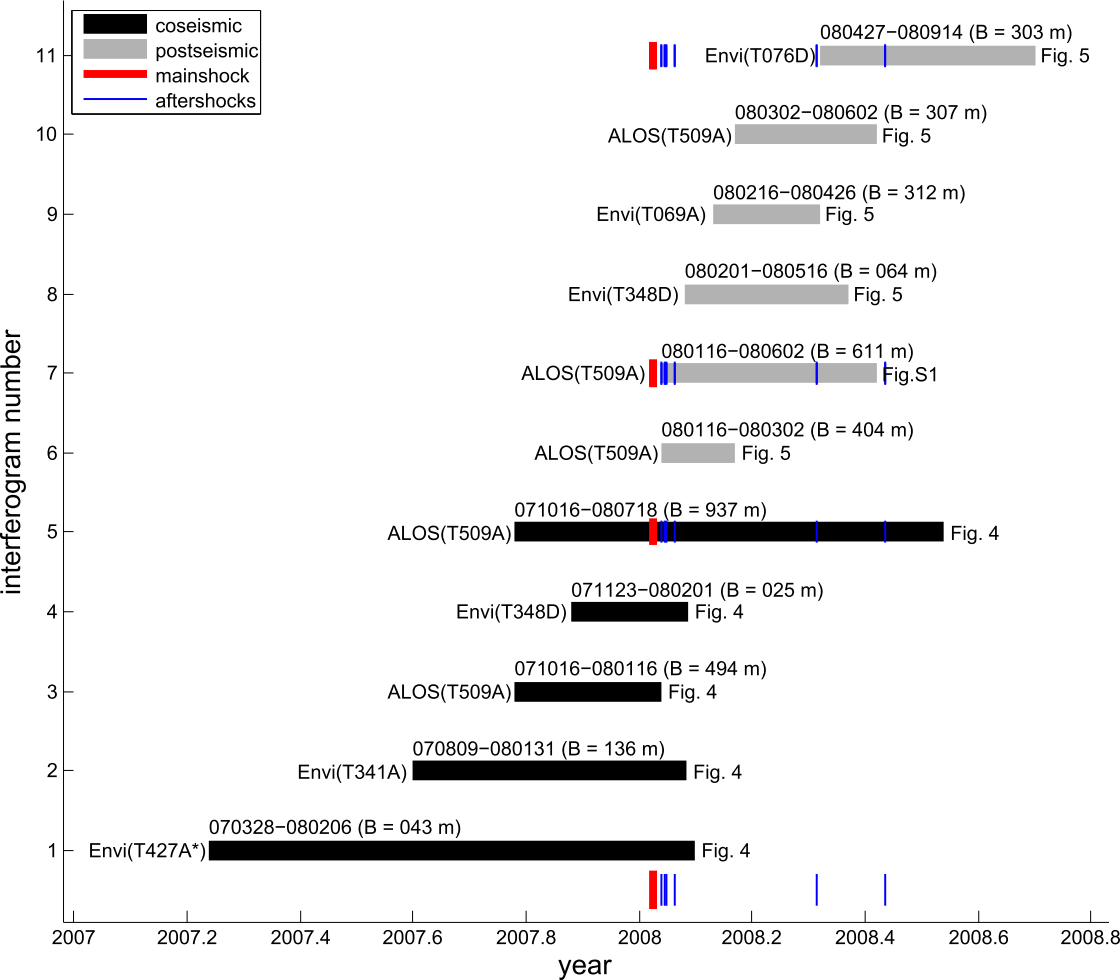
coseismic
postseismic
mainshock
aftershocks
080427−080914 (B = 303 m)
Envi(T076D)
Fig. 5
080302−080602 (B = 307 m)
ALOS(T509A)
Fig. 5
080216−080426 (B = 312 m)
Envi(T069A)
Fig. 5
080201−080516 (B = 064 m)
Envi(T348D)
Fig. 5
080116−080602 (B = 611 m)
ALOS(T509A)
Fig.S1
080116−080302 (B = 404 m)
ALOS(T509A)
Fig. 5
071016−080718 (B = 937 m)
ALOS(T509A)
Fig. 4
071123−080201 (B = 025 m)
Envi(T348D)
Fig. 4
071016−080116 (B = 494 m)
ALOS(T509A)
Fig. 4
070809−080131 (B = 136 m)
Envi(T341A)
Fig. 4
070328−080206 (B = 043 m)
Envi(T427A*)
Fig. 4
interferogram number
year
2007
2007.2
2007.4
2007.6
2007.8
2008
2008.2
2008.4
2008.6
2008.8
1
2
3
4
5
6
7
8
9
10
11

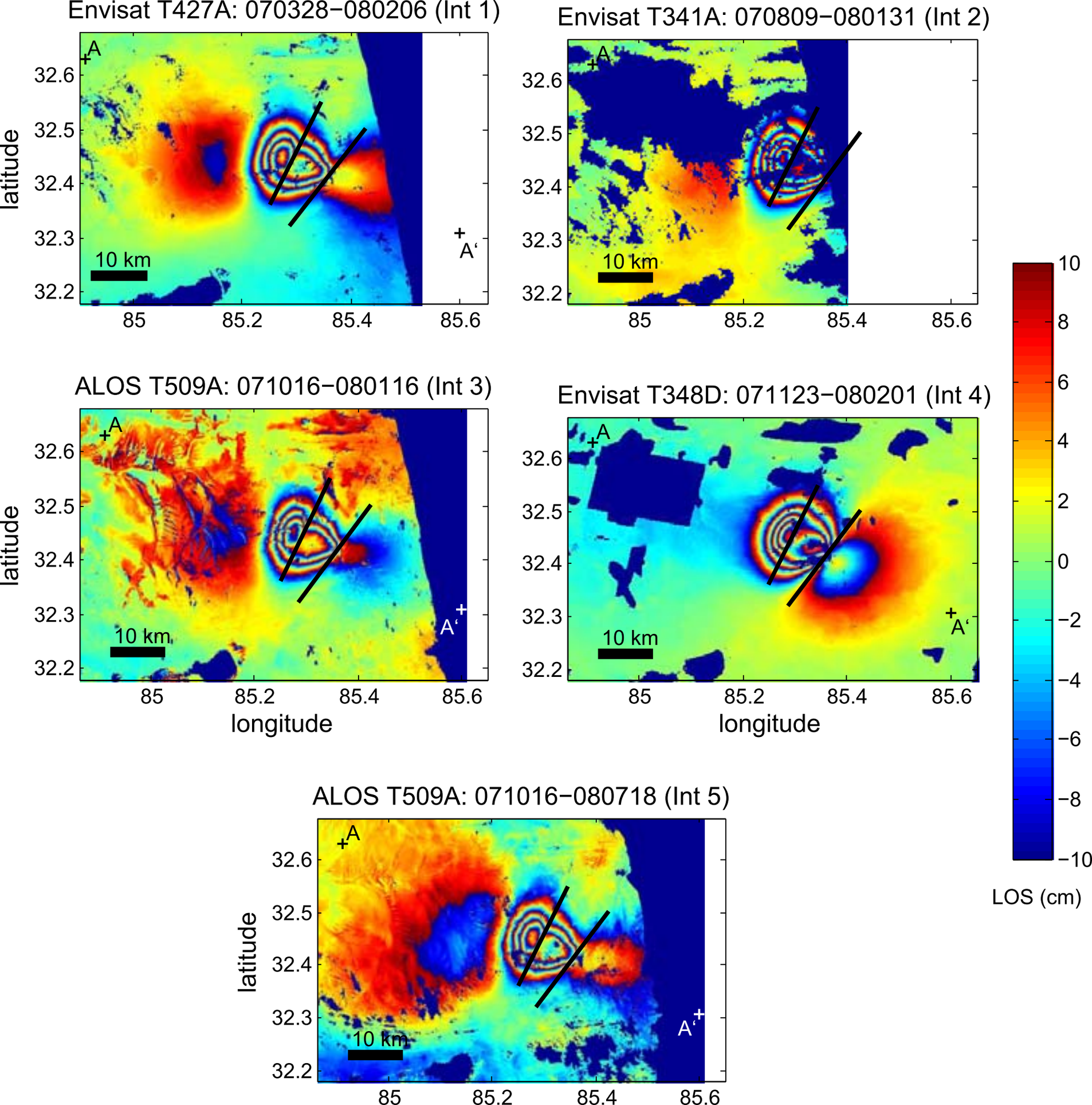
Envisat T427A: 070328−080206 (Int 1)
Envisat T341A: 070809−080131 (Int 2)
ALOS T509A: 071016−080116 (Int 3)
Envisat T348D: 071123−080201 (Int 4)
ALOS T509A: 071016−080718 (Int 5)
A
A'
10 km
latitude
longitude
32.2
32.3
32.4
32.5
32.6
85
85.2
85.4
85.6
10
8
6
4
2
0
−2
−4
−6
−8
−10
LOS (cm)

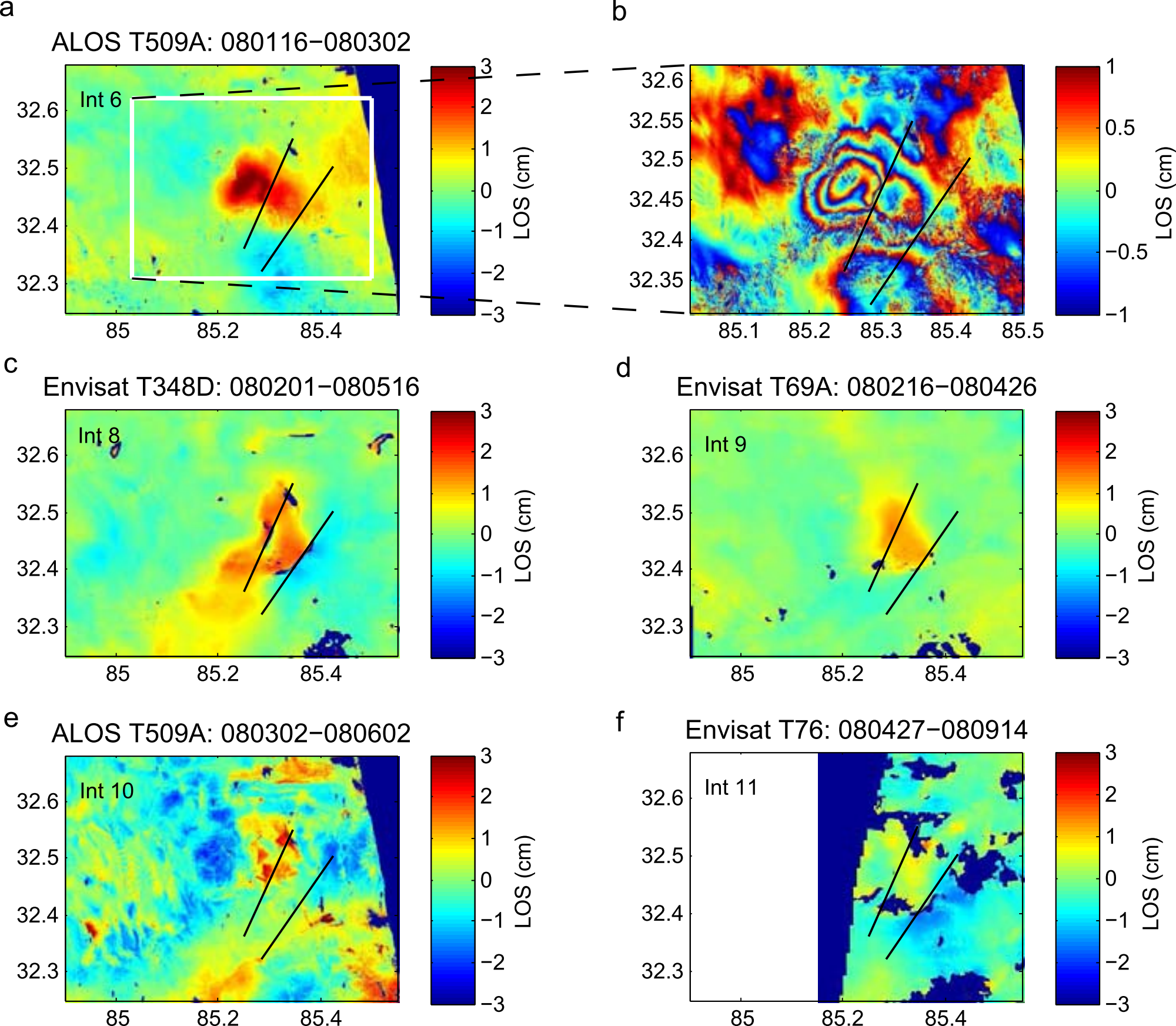
a
ALOS T509A: 080116−080302
Int 6
b
c
Envisat T348D: 080201−080516
Int 8
d
Envisat T69A: 080216−080426
Int 9
e
ALOS T509A: 080302−080602
Int 10
f
Envisat T76: 080427−080914
Int 11
LOS (cm)

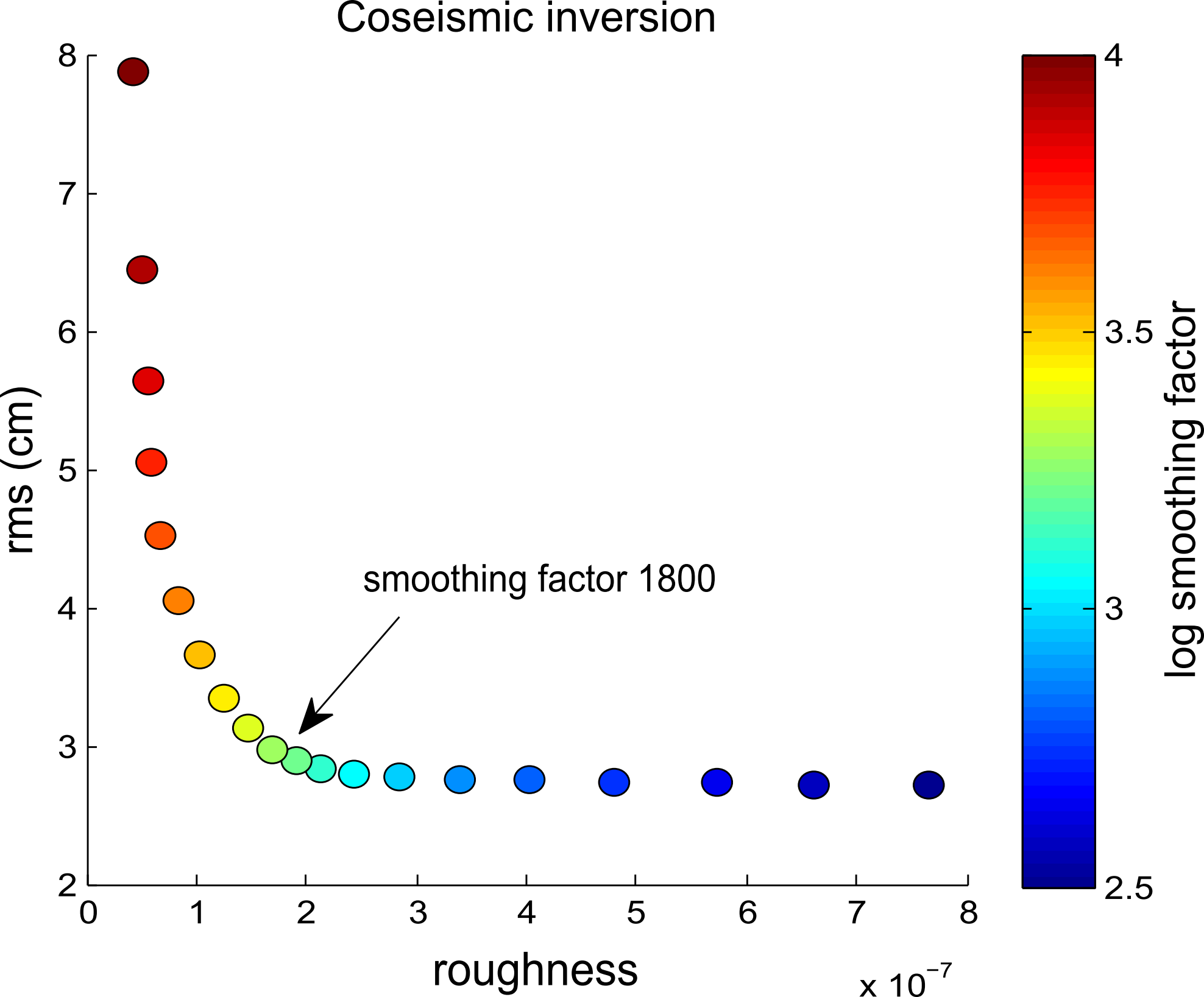
Coseismic inversion
rms (cm)
roughness
x 10^-7
smoothing factor 1800
log smoothing factor
8
7
6
5
4
3
2
0
1
2
3
4
5
6
7
8
4
3.5
3
2.5

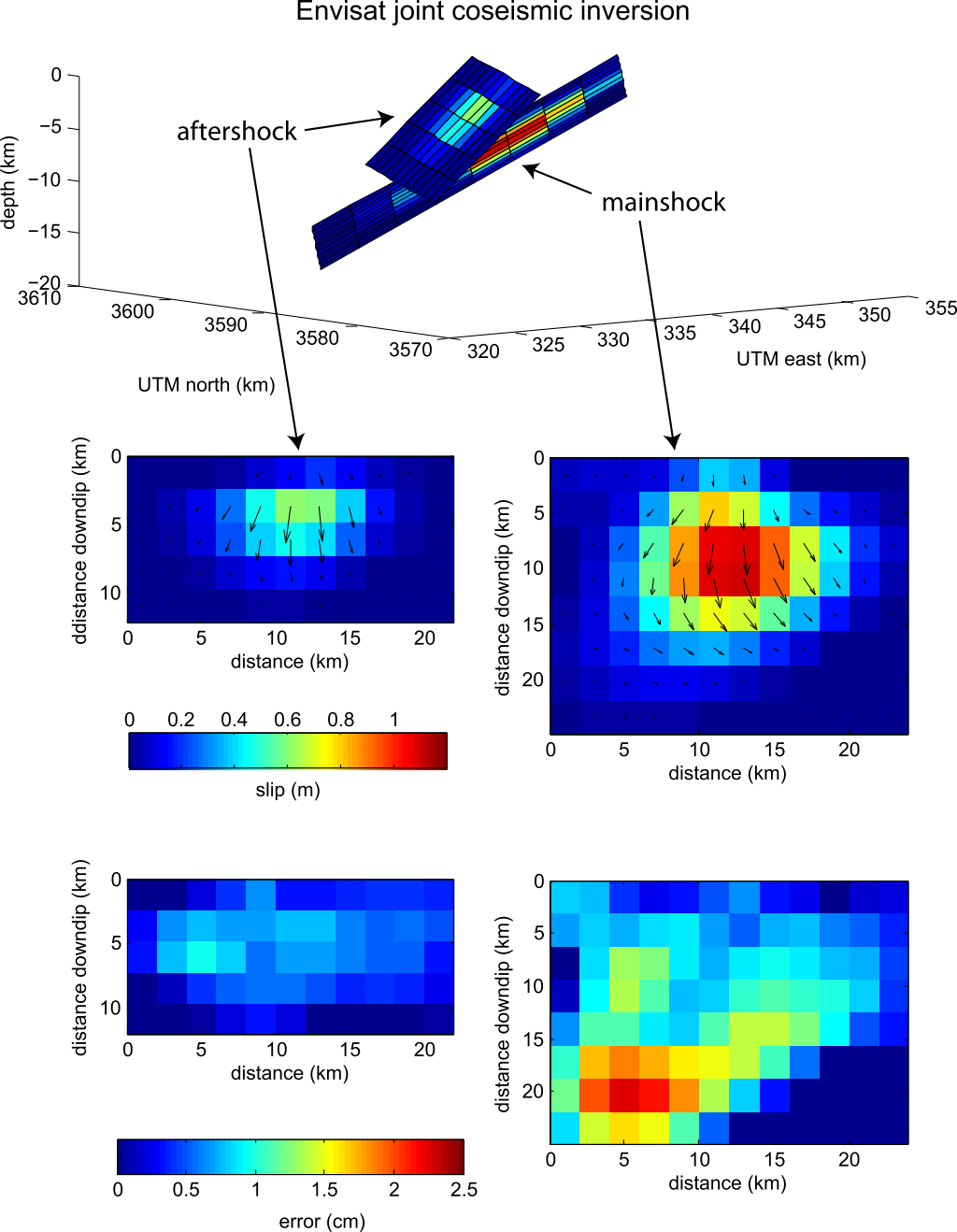
Envisat joint coseismic inversion
aftershock
mainshock
depth (km)
0
−5
−10
−15
−20
3610
3600
3590
3580
3570
UTM north (km)
320
325
330
335
340
345
350
355
UTM east (km)
ddistance downdip (km)
distance (km)
distance downdip (km)
0
0.2
0.4
0.6
0.8
1
slip (m)
error (cm)
0
0.5
1
1.5
2
2.5

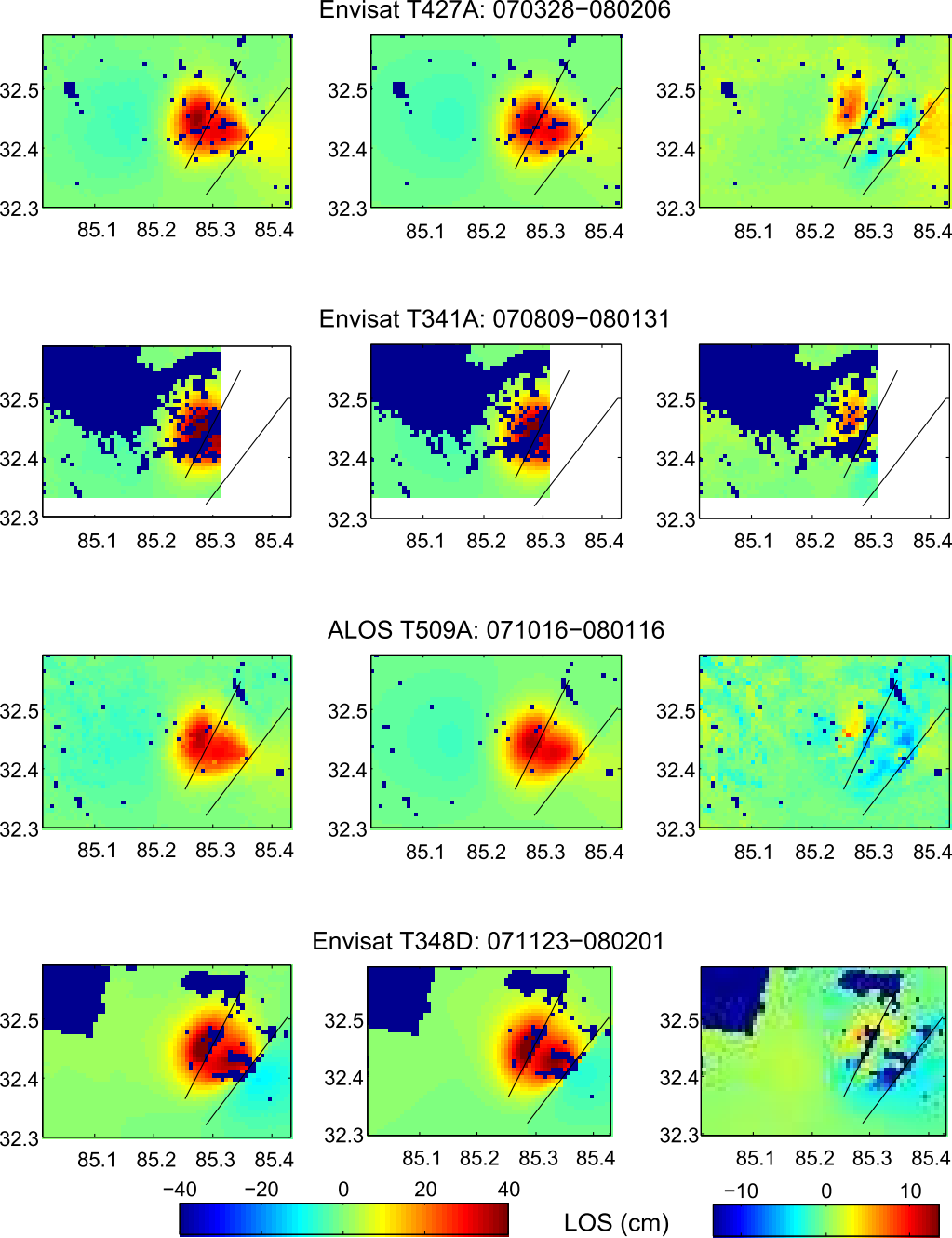
Envisat T427A: 070328−080206
Envisat T341A: 070809−080131
ALOS T509A: 071016−080116
Envisat T348D: 071123−080201
32.5
32.4
32.3
85.1
85.2
85.3
85.4
−40
−20
0
20
40
−10
0
10
LOS (cm)

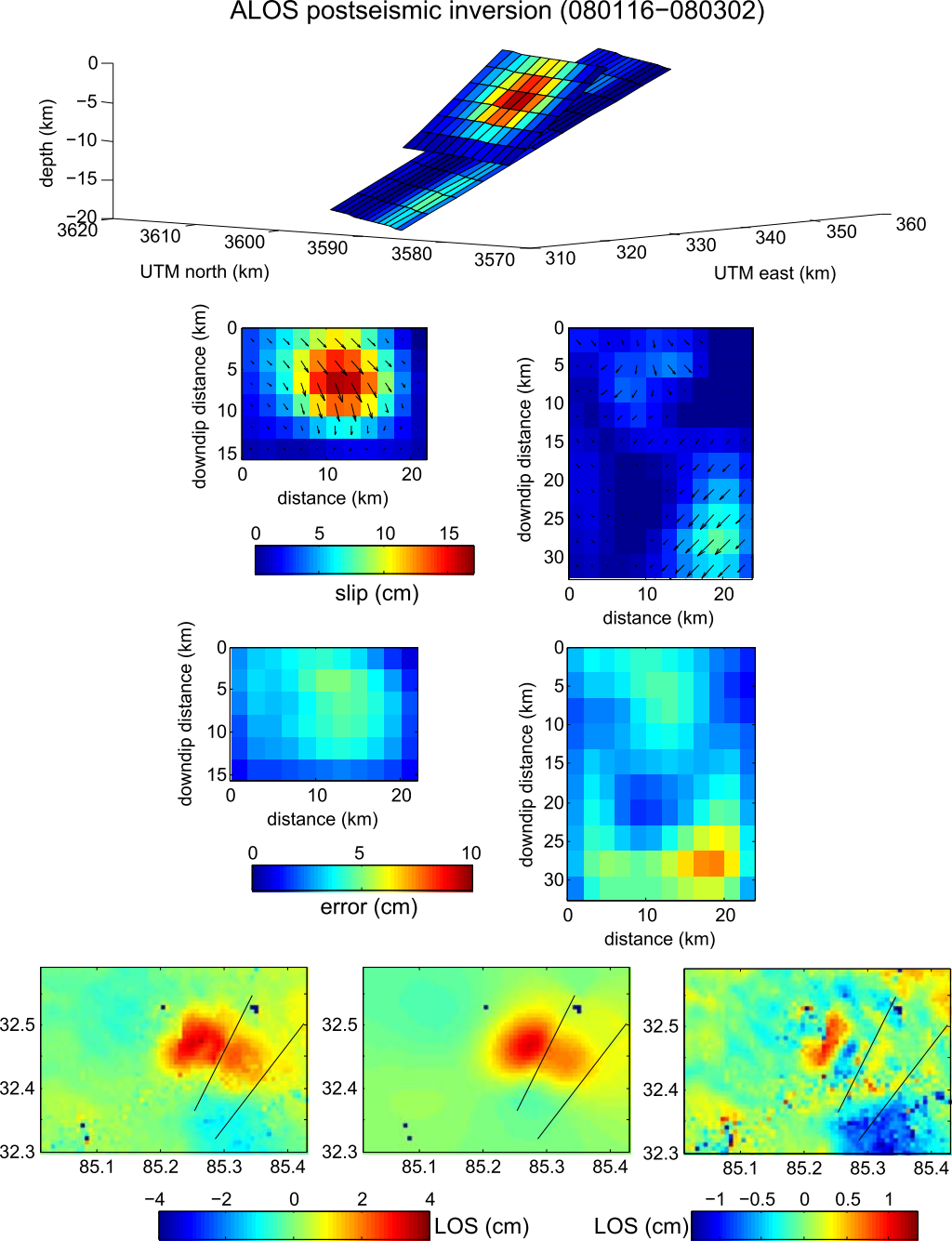
ALOS postseismic inversion (080116−080302)
depth (km)
0
−5
−10
−15
−20
3620
3610
3600
3590
3580
3570
UTM north (km)
310
320
330
340
350
360
UTM east (km)
downdip distance (km)
distance (km)
0
5
10
15
20
25
30
slip (cm)
error (cm)
32.5
32.4
32.3
85.1
85.2
85.3
85.4
−4
−2
0
2
4
LOS (cm)
−1
−0.5
0.5
1

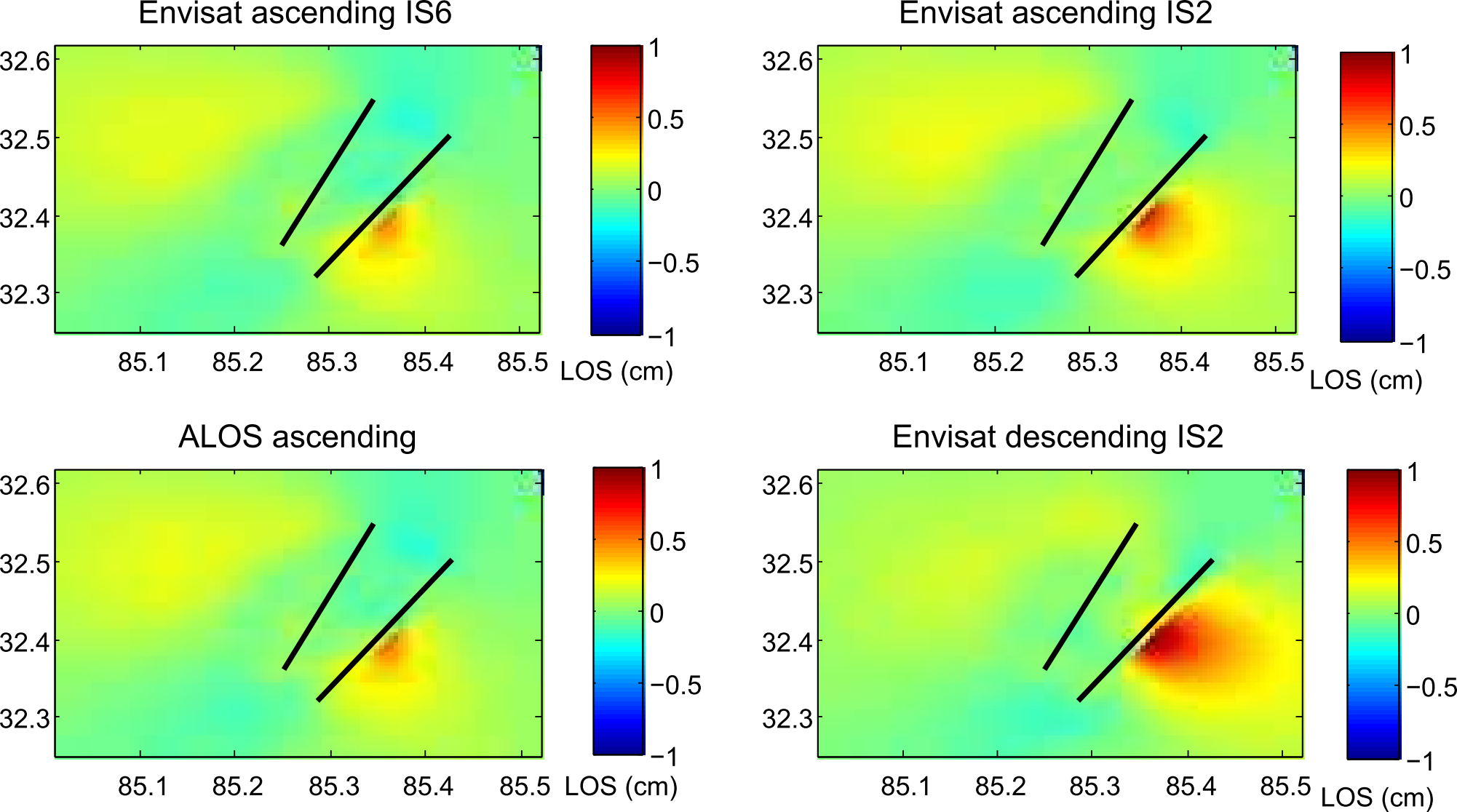
Envisat ascending IS6
Envisat ascending IS2
ALOS ascending
Envisat descending IS2
32.6
32.5
32.4
32.3
85.1
85.2
85.3
85.4
85.5
1
0.5
0
−0.5
−1
LOS (cm)

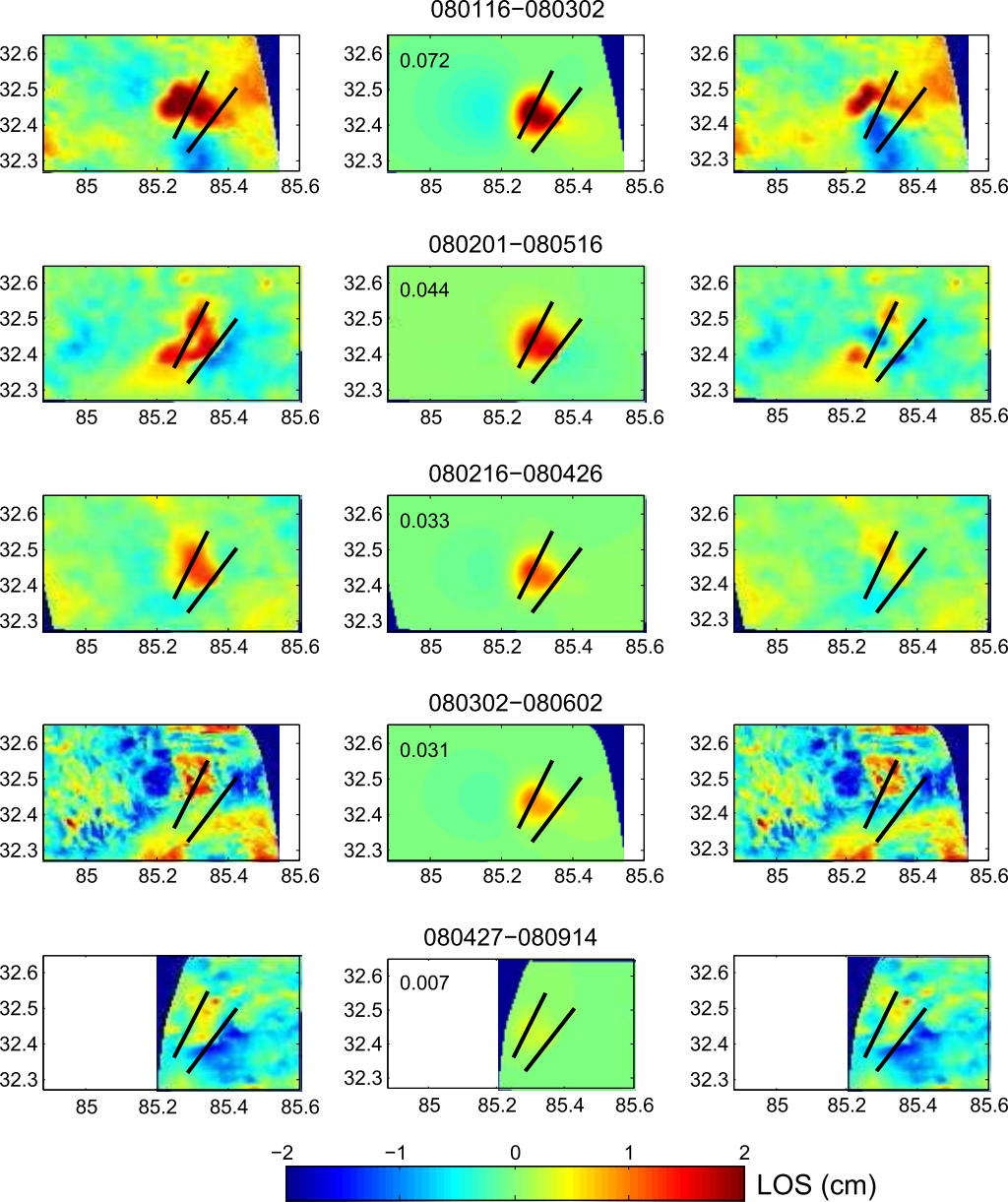
080116−080302
0.072
080201−080516
0.044
080216−080426
0.033
080302−080602
0.031
080427−080914
0.007
32.6
32.5
32.4
32.3
85
85.2
85.4
85.6
−2
−1
0
1
2
LOS (cm)

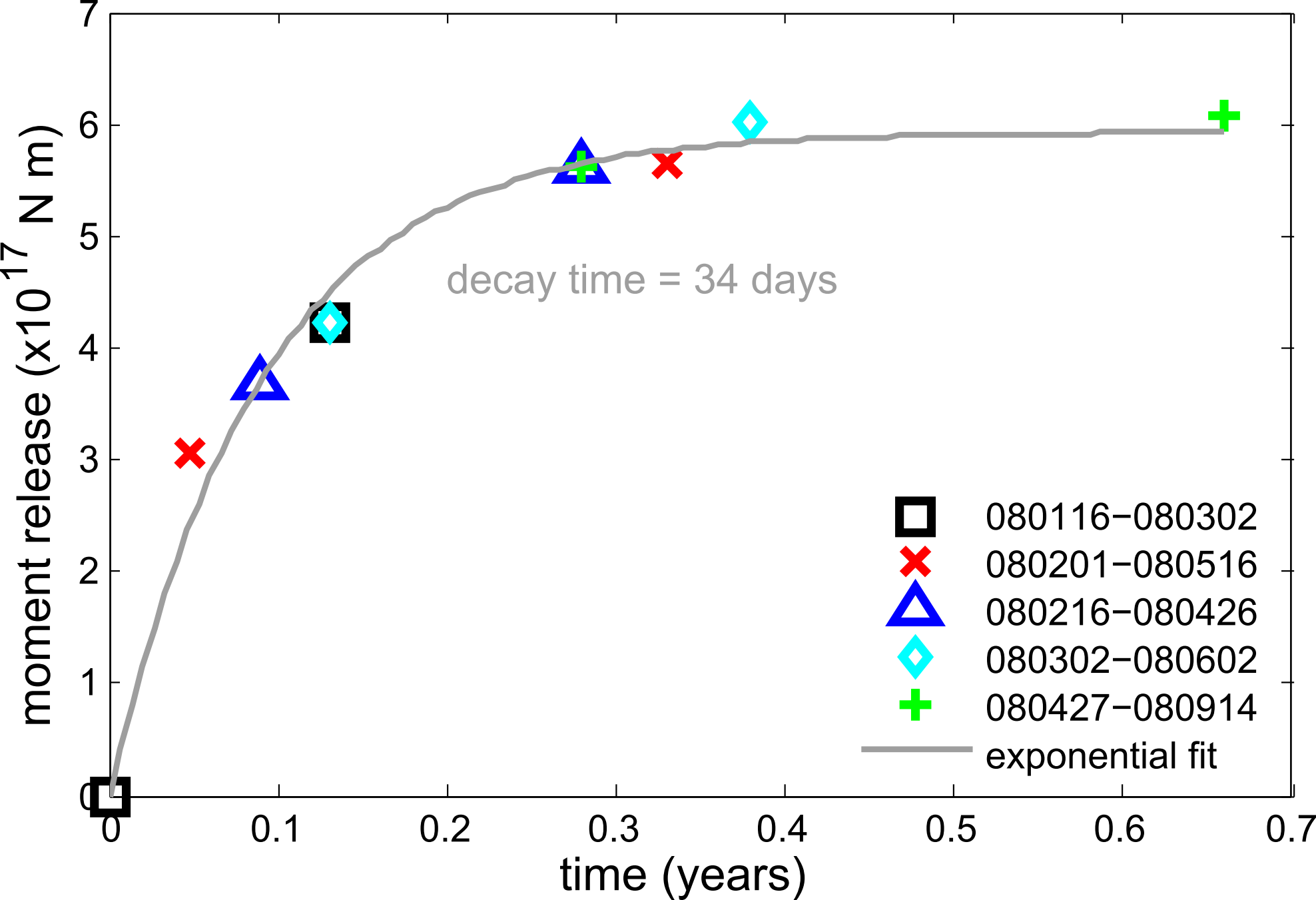
moment release (x10^17 N m)
time (years)
decay time = 34 days
080116−080302
080201−080516
080216−080426
080302−080602
080427−080914
exponential fit
0
1
2
3
4
5
6
7
0
0.1
0.2
0.3
0.4
0.5
0.6
0.7

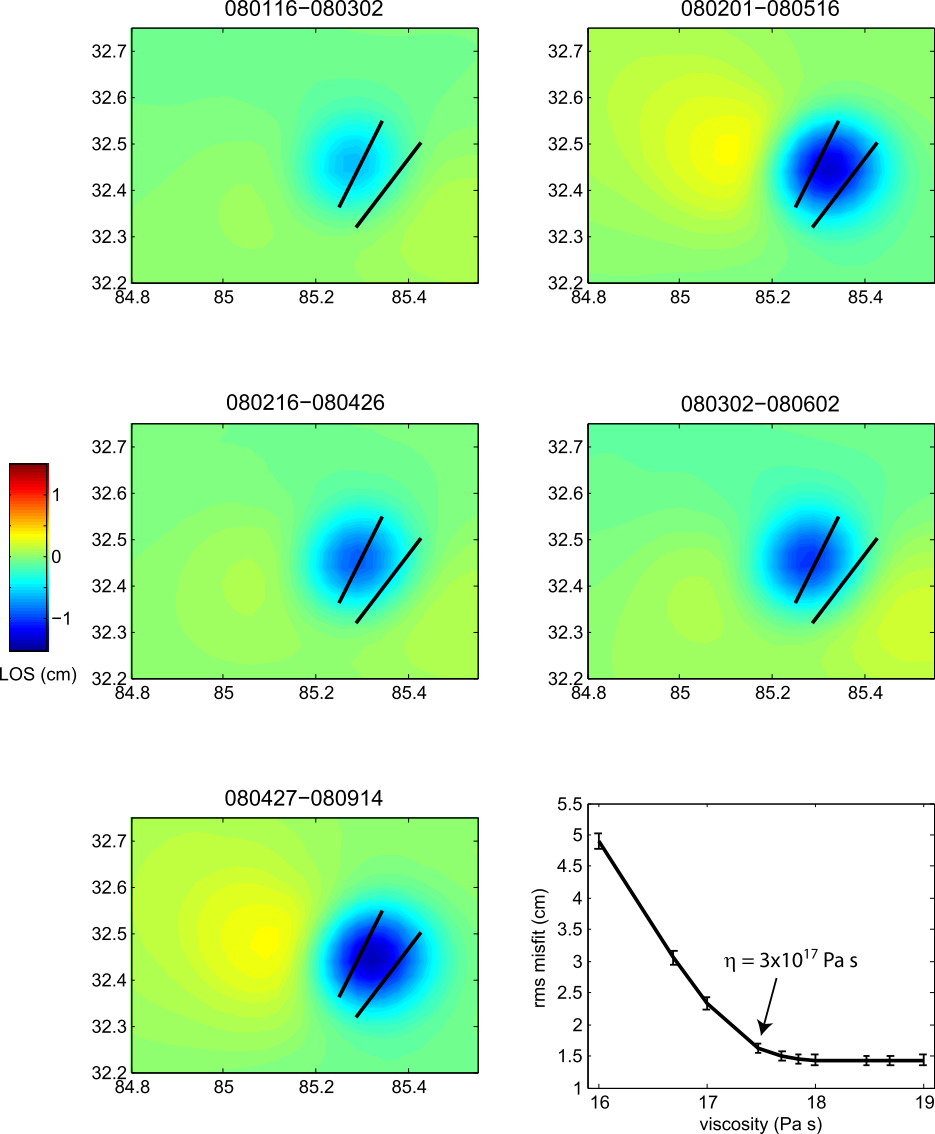
080116−080302
080201−080516
080216−080426
080302−080602
080427−080914
32.7
32.6
32.5
32.4
32.3
32.2
84.8
85
85.2
85.4
1
0
−1
LOS (cm)
5.5
5
4.5
4
3.5
3
2.5
2
1.5
1
rms misfit (cm)
η = 3x10^17 Pa s
16
17
18
19
viscosity (Pa s)